

RXTE Spectral Observations of the 1996–97 Outburst of the Microquasar GRO J1655–40

Gregory J. Sobczak

Astronomy Dept., Harvard University, 60 Garden St., Cambridge, MA 02138;
gsobczak@cfa.harvard.edu

Jeffrey E. McClintock

Harvard-Smithsonian Center for Astrophysics, 60 Garden St., Cambridge, MA 02138;
jem@cfa.harvard.edu

Ronald A. Remillard

Center for Space Research, MIT, Cambridge, MA 02139; rr@space.mit.edu

Charles D. Bailyn

Department of Astronomy, Yale University, P. O. Box 208101, New Haven, CT 06520;
bailyn@astro.yale.edu

Jerome A. Orosz

Dept. of Astronomy and Astrophysics, The Pennsylvania State University, 525 Davey
Laboratory, University Park, PA 16802; orosz@astro.psu.edu

ABSTRACT

Excellent coverage of the entire 16-month 1996–97 outburst cycle of GRO J1655–40 was provided by the *Rossi X-ray Timing Explorer*. We present a full spectral analysis of these data, which includes 52 Proportional Counter Array spectra from 2.5–20 keV and High Energy X-ray Timing Experiment spectra above 20 keV. We also include a nearly continuous All-Sky Monitor light curve with several intensity measurements per day. The data are interpreted in the context of the multicolor blackbody disk/power-law model. The source exhibits two principal outburst states which we associate with the very high and the high/soft states. During the very high state, the spectrum is often dominated by a power-law component with photon index (Γ) \sim 2.3–2.7. The source exhibits intense hard flares on time scales of hours to days which are correlated with changes in both the fitted temperature and radius of the inner accretion disk. During the high/soft state, the spectrum is dominated by the soft thermal emission from the accretion disk with spectral parameters that suggest approximately constant inner disk radius and temperature. The power-law

component is relatively weak with $\Gamma \sim 2\text{--}3$. During the last few observations, the source undergoes a transition to the low/hard state.

We find that a tight relationship exists between the observed inner radius of the disk and the flux in the power-law component. During intense hard flares, the inner disk radius is observed to decrease by as much as a factor of three on a time scale of days. The apparent decrease of the inner disk radius observed during the flares may be due to the failure of the multicolor disk model caused by a steepening of the radial temperature profile in the disk coupled with increased spectral hardening and not physical changes of the inner disk radius. The distortion of the inner disk spectrum by the power-law flares indicates that the physical mechanism responsible for producing the power-law emission is linked to the inner disk region.

Assuming that our spectral model is valid during periods of weak power-law emission, our most likely value for the inner disk radius implies $a_* < 0.7$. Such a low value for the black hole angular momentum is inconsistent with the relativistic frame dragging and the ‘diskoseismic’ models as interpretations for the 300 Hz X-ray QPO seen during some of these RXTE observations.

Subject headings: black hole physics — stars: individual(GRO J1655-40) — stars: individual(Nova Muscae 1991) — stars: individual(GRS 1915+105) — X-rays: stars

1. Introduction

The X-ray Nova GRO J1655–40 was discovered 1994 July 27 (UT) by the Burst and Transient Source Experiment (BATSE) onboard the *Compton Gamma Ray Observatory* (Zhang et al. 1994). The optical counterpart was discovered soon thereafter by Bailyn et al. (1995). It was subsequently found that GRO J1655–40 contained a black hole primary with mass $7.02 \pm 0.22 M_\odot$ (Orosz & Bailyn 1997; van der Hooft et al. 1998), the most accurately measured mass for any black hole candidate. GRO J1655–40 is one of only eight Black Hole X-ray Novae (BHXN) with a dynamically determined primary mass that exceeds $3 M_\odot$, the maximum mass of a neutron star (Kalogera & Baym 1996; McClintock 1998). GRO J1655–40 is one of a few Galactic X-ray sources known to produce superluminal radio jets (Tingay et al. 1995; Hjellming & Rupen 1995). The others are GRS 1915+105, which is also suspected of being a black hole (Mirabel & Rodriguez 1994,1998), and possibly Cyg X-3 (Mioduszewski et al. 1997; Newell et al. 1998). These sources, and a few other Galactic

X-ray sources that exhibit double-lobed radio structures (e.g. 1E1740.7–2942; see Smith et al. 1997 and references therein), are known collectively as the ‘microquasars’, since they have properties analogous to radio-loud active galactic nuclei. GRO J1655–40 is also of intense current interest because it has been proposed to be a rapidly rotating Kerr black hole based on its spectral characteristics (Zhang, Cui, & Chen 1997a) and on the frame dragging model for the observed 300 Hz QPO (Cui, Zhang, & Chen 1998).

The X-ray behavior of BHXN can be described in terms of five distinct, canonical spectral states characterized by the presence or absence of a soft blackbody component at ~ 1 keV and the properties of a power-law component at higher energies above ~ 10 keV. In order of increasing luminosity, these states are the *quiescent/off*, *low/hard*, *intermediate*, *high/soft*, and *very high* states. The *quiescent/off* state is characterized by an X-ray luminosity several orders of magnitude lower than the other states, and a power-law spectrum with a photon index ~ 2 (Narayan, Barret & McClintock 1997). The *low/hard* state consists of a power-law component with photon index $\Gamma \sim 1.4$ – 1.9 with an exponential cutoff ~ 100 keV and a weak thermal component. Sources in the *low/hard* state exhibit strong variability at frequencies $\lesssim 10$ Hz (van der Klis 1995). The *high/soft* state is dominated by a soft ~ 1 keV blackbody component due to a hot accretion disk (Tanaka & Shibazaki 1996) and a power-law with $\Gamma \sim 2.2$ – 2.7 . The *high/soft* state has an X-ray luminosity $L_x \sim 0.2$ – $0.3 L_{Edd}$ compared to $L_x \lesssim 0.1 L_{Edd}$ for the *low/hard* state (Nowak 1995). Sources in the *high/soft* state exhibit little temporal variability (van der Klis 1995). The *intermediate* state, as evidenced by its name, has properties in common with both the *low/hard* and *high/soft* spectral states. The intermediate state has been observed as a distinct spectral state in Nova Muscae 1991 (Ebisawa et al. 1994), Cyg X-1 (Belloni et al. 1996), and GX 339–4 (Mendez & van der Klis 1997). The *very high* state spectrum has a dominant power-law component with photon index ~ 2.5 and exhibits strong variability and high X-ray luminosity, $L_x \sim L_{Edd}$ (Ebisawa et al. 1994). Sources in the *very high* state exhibit quasi-periodic oscillations (QPOs) near 3–10 Hz and at frequencies as high as 300 Hz (van der Klis 1995; Remillard et al. 1998). Thermal emission from the disk remains visible in the *very high* state.

In this paper we present the spectral results for 52 pointed observations which cover the entire 16-month 1996–97 outburst of GRO J1655–40 and employed all the instruments aboard the *Rossi X-ray Timing Explorer* (RXTE): namely, the All-Sky Monitor (ASM), the Proportional Counter Array (PCA), and the High Energy X-ray Timing Experiment (HEXTE). Our results consist of ASM lightcurves, 52 detailed PCA spectra from 2.5–20 keV, and HEXTE spectra above 20 keV when the hard X-ray count rate was sufficient. The spectra were fit to a model including interstellar absorption, multicolor blackbody disk, and power-law components. A timing study based on these same RXTE

observations of GRO J1655–40 is presented in a companion paper (Remillard et al. 1998).

The observations are discussed in § 2, and the results of the spectral fitting are presented in § 3. Section 4 highlights the correlations between the disk and power-law components with a discussion of the limitations of the multicolor disk model and the interpretation of the fitted inner disk radius. Section 5 contains a discussion of the Zhang et al. (1997a) corrections to the observed spectral parameters due to general relativistic effects and an estimate of the black hole angular momentum. The relation between the observed spectral parameters and QPOs is discussed in § 6 followed by a brief summary of our results.

The units used in this paper are $r = R/r_g$ where $r_g = GM/c^2$, $m = M/M_\odot$, $l = L/L_{Edd}$ where $L_{Edd} = 1.25 \times 10^{38} \text{ m erg s}^{-1}$ is the Eddington luminosity, and $\dot{m} = \dot{M}/\dot{M}_{Edd}$, where $\dot{M}_{Edd} = L_{Edd}/(0.1c^2) = 1.39 \times 10^{18} \text{ m g s}^{-1}$ is the Eddington accretion rate, assuming an accretion efficiency of 10%.

2. Observations & Reductions

We present observations covering the entire 16 month 1996–97 outburst of GRO J1655–40 obtained using the ASM, PCA, and HEXTE instruments onboard RXTE. The ASM has three energy channels corresponding to 1.5–3 keV, 3–5 keV, and 5–12 keV (Levine et al. 1996). The PCA data were taken in the “Standard 2” format which corresponds to 129 energy channels from 0–100 keV. The PCA contains five individual proportional counter units (PCUs 0–4). The response matrix for each PCU was obtained from the 1997 October 2 distribution of response files from Keith Jahoda’s ftp site on heaftp.gsfc.nasa.gov. The application of more recent response files (1998 January) to a few of our observations shows that the fit parameters differ by less than 5%.

The spectrum from each PCU was fit individually over the energy range 2.5–20 keV, including a systematic error in the count rates of 1.5%. The good energy range was decided by trial-and-error fitting of archival observations of the Crab Nebula (1997 July 26 & 1997 March 22) and the data set presented here. The lower limit of 2.5 keV was used because of uncertainty in the response at lower energies, and the upper limit of 20 keV was used because there are systematic problems (at the level of a few percent) in the response matrices and background subtraction near 25 keV. The PCA spectra were background subtracted using the standard background model for bright sources, which includes corrections for the instantaneous particle flux, activation, and the cosmic X-ray background. We found that PCUs 2 & 3 yielded reduced chi-squared (χ_ν^2) values consistently higher than PCUs 0, 1, &

4 for fits to archival observations of the Crab Nebula. In addition, we found that PCU 4 gave consistently lower count rates ($\sim 3\%$) than PCUs 0 & 1 at low energies ($\lesssim 6$ keV). Consequently, only PCUs 0 & 1 were used for the spectral fitting reported here and both PCUs were fit simultaneously using XSPEC.

The standard HEXTE reduction software was used for the extraction of the HEXTE data. We used the HEXTE response matrices released 1997 March 20. Only the data above 20 keV was used because of uncertainty in the response at lower energies. The HEXTE modules were alternately pointed every 32 s at source and background positions, allowing background subtraction with high sensitivity to time variations in the particle flux at different positions in the spacecraft orbit. The HEXTE normalization is allowed to float independent of the PCA normalization since there is a $\sim 20\%$ systematic offset between the two instruments in the normalization for the Crab nebula, part of which is due to uncertainties in the deadtime for the HEXTE instrument. All of the normalizations reported here were obtained from the PCA data.

3. Analysis & Results

The total ASM lightcurve (2–12 keV) and the ASM spectral hardness ratio, HR2, are plotted in Figures 1a & b. The origin of time was chosen such that day zero corresponds to the initial rise in the X-ray intensity in the ASM: day 0 = MJD 50198 = 1996 April 25 (UT) (Orosz et al. 1997) (MJD = JD – 2,400,000.5). The lightcurve exhibits erratic flaring from approximately day 27 to 147 and again from day 175 to day ~ 200 . The flaring ceases shortly before the gap in the data around day 220, which is when the source moved into the solar exclusion zone (SEZ). The (5–12 keV)/(3–5 keV) ratio is roughly constant following passage through the SEZ, except for a dip followed by a sharp hardening of the spectrum near day 470. After day 470, the PCA data show (see below) that the source enters the low/hard state; it is then too faint to detect with the ASM. The outburst of GRO J1655–40 evolves through a succession of three of the canonical spectral states (very high, high/soft, and low/hard), as indicated in Figure 1a. The states are defined by the timing behavior and spectral characteristics of each state. Sample spectra from each of these states are plotted in Figure 2, along with the best fit models for each spectrum. Mendez, Belloni, & van der Klis (1998) identified three states during the decay of the outburst using some of the same observations presented here.

The PCA/HEXTE spectral data were fit using XSPEC to a model of interstellar absorption using the Wisconsin cross-sections (Morrison & McCammon 1983) plus a multicolor blackbody accretion disk (Mitsuda et al. 1984; Makishima et al. 1986) plus a

power-law component. In addition, a smeared Fe absorption edge or a Compton reflection component were applied in particular cases, as described below. The hydrogen column density was fixed at 0.89×10^{22} atoms per cm^{-2} (Zhang et al. 1997b).

The multicolor disk + power-law model is widely used and well established (Tanaka & Lewin 1995, and references therein; Ebisawa et al. 1994). Some assumptions and limitations of the model are discussed in § 4 and figure prominently in our interpretation of the observed changes in the inner disk radius. We attempted to use several alternative models to fit the observed spectra. Combinations of disk blackbody, power-law, thermal bremsstrahlung, and comptonization models resulted either in values of χ^2_ν several times larger than the multicolor disk + power-law model or gave unphysical values for the fit parameters.

The four principle quantities returned from the fits were the power-law photon index (Γ), the power-law normalization (K) in units of photons $\text{s}^{-1} \text{cm}^{-2} \text{keV}^{-1}$ at 1 keV, the color temperature of the inner accretion disk (T_{col}) in keV, and the multicolor disk normalization parameter:

$$\left(\frac{R_{col}}{km}\right)^2 / \left(\frac{D}{10 kpc}\right)^2 \cos \theta, \quad (1)$$

where R_{col} is the inner disk radius in kilometers derived from the color temperature, D is the distance to the source in kiloparsecs, and θ is the inclination angle of the system. The mass, inclination angle, and distance of GRO J1655–40 are well determined: $M = 7.02 \pm 0.22 M_\odot$, $\theta = 69.5 \pm 0.1$ (Orosz & Bailyn 1997), and $D = 3.2 \pm 0.2$ kpc (Hjellming & Rupen 1995). Substituting these values into equation (1) allows us to solve for R_{col} in units of $r_{col} = R_{col}/r_g$ where $r_g = GM/c^2 = 10.4$ km.

T_{col} & r_{col} (usually referred to in the literature as T_{in} & r_{in}) are often taken to be the temperature and radius of the inner accretion disk. However, corrections for spectral hardening must be made to the observed spectral parameters (T_{col} & r_{col}) to determine the effective temperature and radius of the inner disk (T_{eff} & r_{eff}). These corrections compensate for the fact that electron scattering dominates over absorption as a source of opacity in the disk and affects the inner disk spectrum through Comptonization of the emergent spectrum (Shakura & Sunyaev 1973). Such a Comptonized spectrum may be approximated by a diluted blackbody (Ebisawa et al. 1994):

$$I(E) = \left(\frac{1}{f^4}\right) B(T_{col}, E), \quad (2)$$

where $B(T_{col}, E)$ is the Planck function, T_{col} is the color temperature, and f is the color correction or spectral hardening factor. In this diluted blackbody spectrum, the spectral

shape is the same as a blackbody with temperature $T_{col} = fT_{eff}$, where T_{eff} is the effective temperature (also called T_{peak} or T_{max}), and the normalization is smaller by the factor $1/f^4$. Since the normalization fit by the multicolor disk model is proportional to r_{col}^2 (see Eq. (1)), the actual radius should be f^2 times larger than obtained from fitting the multicolor disk model.

Shimura & Takahara (1995) have shown, using a numerical simulation which self-consistently solves for the vertical structure and radiative transfer in the accretion disk, that the spectral hardening factor $f = (T_{col}/T_{eff})$ can be approximated by a constant $f = 1.7 \pm 0.2$ for $\alpha_v \sim 0.1$, $1.4 \leq m \leq 10$, and $0.1 \leq \dot{m} \leq 10$, where α_v is the viscosity parameter. Therefore, the fit values of T_{col} and r_{col} can be corrected approximately for spectral hardening by using the following formulas:

$$T_{eff} = \frac{T_{col}}{f} = \frac{T_{col}}{1.7}, \quad (3)$$

$$r_{eff} = f^2 r_{col} = 2.9 r_{col}, \quad (4)$$

where T_{eff} and r_{eff} are the effective temperature and radius of the inner accretion disk. The model parameters, corrected for spectral hardening, are listed in Table 1 and presented in Figures 3a–d.

3.1. Very High State

In Figures 1a & 3d, we see that between days 27 and 147, and days 175 and 222, there are sudden flares during which the power-law normalization increases by a factor of ten in only a few days. These flares in the hard component are accompanied by an increase in T_{eff} from ~ 0.76 keV to 1.13 keV (Fig. 3a) and a decrease in r_{eff} from ~ 5.5 to 1.6 (Fig. 3b). There is also an abrupt increase in Γ from ~ 2.3 to 2.7 (Fig. 3c). We identify this flaring behavior with the very high state because of the strong power-law component with $\Gamma \sim 2.5$ and the presence of strong QPOs from 7.3–22.4 Hz (Remillard et al. 1998). Figure 2a shows an example of the spectrum during the flares. Between days 147 and 175 the power-law (hard) flares cease and the photon index decreases to 2.0–2.2. During this time, the effective temperature and radius of the inner disk become steady at $T_{eff} \sim 0.75$ keV and $r_{eff} \sim 5.5$; Figure 2b shows a representative spectrum. Nevertheless, we also identify these observations with the very high state because of the relatively strong power-law component and the presence of QPOs from 7.3–22.4 Hz, (Remillard et al. 1998). The only exceptions are days 154 & 161 at which time the source does not exhibit QPOs. These two observations resemble the high/soft state discussed in § 3.2.

For four observations during the hard flares (days 98, 126, and 191 A & B), the fits were significantly improved by adding a Compton reflection component. The Compton reflection component was calculated using the ‘pexriv’ model in XSPEC version 10 (Magdziarz & Zdziarski 1995). The resulting values of the disk blackbody and power-law parameters did not change significantly, and were independent of the temperature of the reflecting medium. A 6.4 keV iron $K\alpha$ emission line is frequently included with the Compton reflection component in such calculations; however, there was no evidence for 6.4 keV iron $K\alpha$ emission in our spectra. The Compton reflection parameters returned from ‘pexriv’ for the four relevant observations are listed in Table 2.

3.2. High/Soft and Low/Hard States

When the source became observable again after passage through the solar exclusion zone, the power-law normalization had decreased by an order of magnitude relative to the peak values and was typically $\lesssim 5$ photons $\text{s}^{-1} \text{cm}^{-2} \text{keV}^{-1}$ at 1 keV (Fig. 3d). The dramatic hard flares had ceased and the effective temperature and radius of the inner disk had settled down to ~ 0.7 keV and $6.5 r_g$, respectively (Fig. 3a & b). The photon index varied significantly from ~ 2 to 3 over only a few days (Fig. 3c) and the source exhibited little temporal variability (Remillard et al. 1998). We identify this period with the high/soft state. A sample high/soft state spectrum is shown in Figure 2c.

Our initial fits for the high/soft state data were poor ($\chi^2_\nu \sim 1\text{--}4$); however, they were significantly improved by the addition of a smeared Fe absorption edge at 8.0 keV (above the neutral Fe K edge at 7.1 keV) (Ebisawa et al. 1994). Figures 4a–c show the effect of the absorption edge on the ratio data/model for a representative high/soft state spectrum. From Figures 4a–c, it is apparent that the addition of an Fe absorption edge significantly improves the χ^2_ν from 1.44 to 1.04 for an edge at 8.0 keV. The best fit edge energy varied from 7 to 9 keV for different spectra. For consistency the edge was fixed at 8.0 keV with a width of 7 keV and only the Fe optical depth was allowed to float. The presence of an Fe absorption feature in BHXN spectra is well established from observations of Cyg X-1, GS 2023+338, LMC X-1, GS 2000+25 (Inoue 1991), and Novae Muscae 1991 (Ebisawa et al. 1994).

The disk temperature during the high/soft state is approximately constant from days 307 to 364, then there is a slight increase of T_{eff} from 0.67 keV to 0.71 keV over 28 days from days 364 to 398 (Fig. 3a). After this slight rise, T_{eff} decreases from 0.71 keV to 0.60 keV over the next 47 days (Fig. 3a) and r_{eff} increases from 6.3 to 7.1 (Fig. 3b).

On day 455, the disk temperature begins to drop rapidly and decreases from 0.57 keV to 0.26 keV over the final 32 days. By day 476 the multicolor blackbody disk appears only as a soft excess below 5 keV. The spectra at this time are dominated by the power-law component with $\Gamma \sim 1.7$ –2.0 and the source exhibited increased variability and low frequency QPOs (Remillard et al. 1998). These properties are characteristic of the low/hard state. A representative spectrum is presented in Figure 2e. In the last three observations, the inner disk radius appears to decrease, which is probably due to the failure of the spectral hardening correction for $\dot{m} \lesssim 0.1$ (Shimura & Takahara 1995) after day 465. Similar behavior was observed in Nova Muscae 1991 (Ebisawa et al. 1994) during the soft-to-hard transition at late times and is attributed to the same cause. The apparent decrease in r_{eff} after day 465, just prior to turnoff, can be explained by an increase in the spectral hardening factor as the inner disk becomes optically thin, rather than a decrease in the inner disk radius (Ebisawa et al. 1994).

The values of Γ and K for days 14–17 are off the scale used in Figure 3, but are given in Table 1. In this initial group of observations, the spectrum below ~ 10 keV is dominated by a soft thermal component with $T_{eff} \sim 0.7$ keV and by a steep quasi-power-law component with $\Gamma \sim 6$ at higher energies. Since the power-law contributes so little flux above 5 keV, compared to the thermal component, we identify these observations with the high/soft state. A sample spectrum from this period is shown in Figure 2d. The quality of the 2.5–20 keV spectral fits was poor ($\chi^2_{\nu} \sim 5$ –8) during this time. *These spectra resisted all attempts to apply the multicolor disk plus power-law model, including modifications for variable N_H , emission lines, absorption edges, Compton reflection, thermal comptonization, and an exponentially cutoff power-law.* The same difficulty was encountered for six other observations during the high/soft state. As a result, we were forced to fit these spectra using interstellar absorption plus a multicolor disk over the restricted range 2.5–10 keV, and then fix these parameters when fitting the high/soft energy component with a power-law from 15–20 keV. This approach gave satisfactory values of χ^2_{ν} (see Table 1). Figure 2d shows a sample spectrum along with the best fit multicolor disk model for these poorly-fit high/soft state spectra. In Figures 3a–d, the spectra which are not well fit by the multicolor disk blackbody plus power-law model above 10 keV are indicated by open circles; in Table 1 the corresponding entries are flagged by footnotes f and g. Note that the effective temperatures and inner disk radii of these cases are consistent with those of the ‘normal’ high/soft state spectra (Fig. 3a & b).

The Advection Dominated Accretion Flow (ADAF) model (Narayan & Yi 1994) has been used successfully to describe the soft-to-hard transition observed in Nova Muscae 1991 (Esin et al. 1997a) and Cyg X-1 (Esin et al. 1997b). For Nova Muscae 1991, Esin et al. (1997a) predicted that the photon index should have risen sharply to ~ 4 or 5 in

the high/soft state prior to the soft-to-hard transition (see their Fig. 12d), during the time when Ebisawa et al. were unable to fit the power-law component and therefore fixed the photon index (see Ebisawa et al. 1994). Similarly, this prediction of the ADAF model may explain the peculiar spectral behavior of GRO J1655–40 during these observations when the apparent power-law component is steep and poorly-determined.

3.3. Disk and Power-law Component Fluxes and Source Luminosity

Figures 5a–c are plots of the total unabsorbed flux (Fig. 5a), the unabsorbed bolometric flux from the disk blackbody component (Fig. 5b) and the unabsorbed flux from the power-law component (2–100 keV) (Fig. 5c). Figure 5d shows the ratio of the disk blackbody to the total flux. During the flares, the power-law component dominates the spectrum and we see that the increase in the power-law flux (Fig. 5c) is accompanied by a decrease in the flux from the disk (Fig. 5b). When the source moves out of the solar exclusion zone, the power-law flux is less than $5 \times 10^{-9} \text{ erg s}^{-1} \text{ cm}^{-2}$ and the flux from the disk component dominates the spectrum. This behavior is even more apparent in Figure 5d, where the disk flux is plotted as a fraction of the total unabsorbed flux from 2–100 keV. During the hard flares, the power-law dominates the unabsorbed flux, contributing $\sim 70\%$ of the total flux (Fig. 5d). During the calm period (around day 160) between the two flaring episodes, the power-law contributes less than 20% of the flux (Fig. 5d). After passage through the SEZ, the disk emission dominates, contributing around 90% of the total flux (Fig. 5d). After day 465, the power-law again dominates the unabsorbed flux, contributing $\sim 70\%$ of the total (Fig. 5d), indicating that the system has undergone a soft-to-hard transition.

Figures 6a & b show r_{eff} and Γ vs. the luminosity in Eddington units, where $L_{Edd} = 8.78 \times 10^{38} \text{ erg s}^{-1}$ for $m = 7.02$. Figure 6a indicates that r_{eff} decreases dramatically when the luminosity exceeds $l \sim 0.17$ and Figure 6b shows that the photon index is not strongly correlated with luminosity. Both of these results are unexpected for canonical outburst states, for which the parameters vary smoothly (e.g. Ebisawa et al. 1994). Also note from Figure 6 that the luminosity of the source in each outburst state is several times lower than the canonical values discussed in § 1. This data indicates that it is problematic to use absolute luminosity as an indicator of spectral states.

4. Correlations in the Spectral Parameters; Comparisons to Nova Mus 1991 and GRS 1915+105

Figures 3a & b show that during the flares, T_{eff} increases from ~ 0.76 to 1.13 keV, while r_{eff} decreases by a factor of about three from ~ 5.5 to 1.6 . Figure 7a shows the correlation between T_{eff} and r_{eff} , from which it is apparent that T_{eff} increases gradually as r_{eff} decreases. Observations during the very high state are plotted as filled circles and observations during the high/soft state are plotted as open squares. Figure 7b shows a surprising correlation between the power-law flux and r_{eff} . From Figure 7b it is apparent that the power-law flux is strongly correlated with r_{eff} and increases steeply for $r_{eff} \lesssim 5.5$.

Figures 8a & b show T_{eff} and the 2–100 keV power-law flux vs. r_{eff} for Nova Muscae 1991 (calculated from data in Ebisawa et al. 1994). Comparing Figures 7b & 8b, it is apparent that both Nova Muscae 1991 and GRO J1655–40 exhibit the same behavior: the power-law flux increases as r_{eff} decreases.

However, the apparent decrease of the inner disk radius observed during the power-law flares may be caused by the failure of the multicolor disk model instead of physical changes of the inner disk radius. During the hard flares, the disk contributes as little as 30% of the observed flux. Since the power-law component in BHXN spectra likely originates from Compton upscattering of soft disk photons, an increase in power-law emission naturally implies an increase in electron scattering. This in turn increases the distortion (spectral hardening) of the inner disk spectrum through Comptonization of the emergent spectrum. Therefore, we might expect the distortion of the inner disk spectrum to be correlated with the power-law emission, as in Figures 7b & 8b.

Shimura & Takahara (1995) have shown that for $\alpha_v > 0.1$ the inner disk gradually becomes optically thin and the assumption of a constant spectral hardening factor breaks down. The spectral hardening factor (f) can become large (as high as $f \sim 10$ near the inner disk radius in an example given by Shimura & Takahara) and the color temperature can assume a steep radial profile. In such a case, fitting the multicolor disk model to the resulting spectrum and assuming a constant spectral hardening factor yields an inner disk radius which is smaller than the physical value. *The apparent decrease of the inner disk radius observed during periods of increased power-law emission may be caused by a steepening of the radial temperature profile of the accretion disk coupled with increased spectral hardening; thus, this apparent decrease does not necessarily represent a physical change of the inner disk radius.*

This interpretation implies that the physical mechanism responsible for producing the power-law emission is linked to the inner disk region and that the relativistic electrons are

produced very near the inner accretion disk. Moreover, it is reasonable that the hard X-ray spectrum will also be produced in the inner disk region since there is a copious supply of soft seed photons there.

GRS 1915+105 and GRO J1655–40 are among the few Galactic sources known to produce superluminal radio jets (Mirabel & Rodriguez 1994, 1998; Tingay et al. 1995; Hjellming & Rupen 1995). Although no dynamical mass estimate for the compact primary in GRS 1915+105 exists, both sources are suspected of containing rapidly rotating black holes (Zhang et al. 1997a; Cui et al. 1998). Furthermore, GRS 1915+105 and GRO J1655–40 have exhibited large changes in the observed temperatures and radii of their inner accretion disks. Belloni et al. (1997a,b) explain the behavior of GRS 1915+105 by the removal and replenishment of the matter forming the inner part of an optically thick disk, probably caused by a Lightman-Eardley type thermal-viscous instability (Lightman & Eardley 1974) analogous to the limit cycle instability in dwarf novae.

The thermal instability model of Belloni et al. (1997a,b) describes the behavior of GRS 1915+105 well, but it cannot account for the variability time scale of GRO J1655–40. The flares in GRS 1915+105 occur on a time scale of ~ 100 seconds, whereas the flares in GRO J1655–40 occur on a time scale of a few days. In the Belloni et al. model, flares are expected to repeat on the time scale necessary to refill the inner disk. In the case of GRO J1655–40, Belloni et al.’s model would predict a flaring time scale of ~ 0.1 seconds, which is some six orders of magnitude shorter than the observed ~ 1 -day flaring time scale. Therefore, the thermal instability model of Belloni et al. cannot be responsible for the flaring behavior observed in GRO J1655–40. Instead, the time scale of the flaring behavior in GRO J1655–40 is comparable to the viscous time scale of the *outer* disk, where the viscous time scale is ~ 1 day for $r \sim 300$. This flaring time scale is close to the 6-day X-ray delay (relative to the optical) that occurred during the 1996 April outburst of GRO J1655–40, which Hameury et al. (1997) identified with the viscous time scale needed to rebuild the inner disk. Changes in the behavior of an accreting system on this time scale can be associated with changes in the mass accretion rate.

5. Spin of the Black Hole

Zhang et al. (1997a) outline general relativistic corrections to the inner disk radius derived from the multicolor disk model for the purpose of determining the true inner disk radius. The angular momentum (a_*) of the black hole can be estimated by equating the inner disk radius with the last stable orbit. In this analysis, the effective temperature of the

disk peaks at a radius

$$r_{eff} = r_{last}/\eta, \quad (5)$$

where r_{last} is the last stable orbit and η is a function of the black hole angular momentum. There is also a general relativistic correction to the spectral hardening factor and an additional change of the observed flux due to viewing angle (Zhang et al. 1997a). However, the inclination angle of GRO J1655–40 makes the general relativistic spectral hardening and viewing angle corrections less than 10% (determined from data in Zhang et al. (1997a)) compared to the $\pm 24\%$ uncertainty in the inner disk radius due to the conventional spectral hardening factor, $f = 1.7 \pm 0.2$ (see Eq. (4)). The important claim of Zhang et al.’s analysis is that r_{eff} is the radius of the peak emission region and not the inner disk radius.

The last stable orbit around a maximally rotating prograde black hole ($a_* = +1$) can extend almost to the event horizon, $GM/c^2 = r_g$, whereas in the nonrotating Schwarzschild case, the last stable orbit is at $6 r_g$. The solutions for r_{eff} , r_{last} , and η , for several values of a_* calculated using the method of Zhang et al. (1997a) are listed in Table 3. It is important to note that this analysis assumes the disk extends all the way down to the last stable orbit, and therefore would not be valid throughout most of the observations presented here if the inner disk radius were actually varying. However, as emphasized in § 4, the apparent decrease of the inner disk radius observed during the power-law flares may be due to the failure of the multicolor disk model and not to physical changes of the inner disk radius.

During the most stable period (from days 307–356), we find the average effective inner disk radius is $r_{eff} = 6.63 \pm 0.04$. It is likely that during this stable period, the disk assumes the steady state $r^{-3/4}$ temperature profile of the standard multicolor disk model, which implies that $r_{eff} = 6.6$ is a good approximation of the actual effective inner disk radius. Applying Zhang et al.’s (1997a) method for $r_{eff} = 6.6$ implies $r_{last} = 4.2$ and $a_* = 0.5$ (Table 3), which is considerably smaller than the results of Zhang et al. who find $a_* = 0.93$.

The dominant source of uncertainty in this calculation (other than systematic uncertainty in the physical interpretation of the disk model) is due to the spectral hardening factor ($f = 1.7 \pm 0.2$), which yields an uncertainty of 24% in the value of r_{eff} (see Eq. (4)). Taking this uncertainty into account, the minimum effective inner disk radius $r_{eff}(min) = 5.0$ corresponds to the upper limit $a_* < 0.7$. Since r_{eff} scales linearly with the assumed distance (see Eq. (1)), applying the firm distance upper limit of 5 kpc from Tingay et al. (1995) and the 24% uncertainty from the spectral hardening factor, we obtain $r_{eff}(max) < 12.9$, which is consistent with a nonrotating (Schwarzschild) black hole (see Table 3).

Using the method adopted here for measuring the inner disk radius, Zhang et al. (1997a) analyzed a single ASCA observation of GRO J1655–40 from 1995 August, during

a previous outburst, and determined that the source contains a rapidly rotating black hole with $a_* = 0.93$, in contrast to our limit of $a_* < 0.7$. However, as demonstrated in § 4, the apparent inner disk radius can vary significantly during outburst. This result emphasizes the importance of obtaining good spectral coverage of the entire outburst cycle.

6. QPOs

It has been proposed that high frequency QPOs in the X-ray lightcurves of BHXN are due to the effects of relativistic frame dragging on an accretion disk orbiting a rotating black hole (Cui et al. 1998). According to this model, the 300 Hz QPO present during the hardest spectral state in GRO J1655–40 (Remillard et al. 1997), implies a specific angular momentum for the black hole of $a_* = 0.95$ for $M = 7 M_\odot$ (Cui et al. 1998). The same model applied to the 67 Hz QPO observed in certain spectral states of GRS 1915+105 (Morgan et al. 1997) also implies a specific angular momentum for the black hole of $a_* = 0.95$ for $M = 30 M_\odot$ (Cui et al. 1998).

In the previous section, we demonstrated that the most likely value of the inner disk radius in GRO J1655–40 implies $a_* < 0.7$ and is consistent with a nonrotating (Schwarzschild) black hole. This result implies that the 300 Hz QPO in GRO J1655–40 probably cannot be due to relativistic frame dragging, which requires a rapidly rotating ($a_* \sim 0.95$) black hole. The low black hole angular momentum in GRO J1655–40 is also inconsistent with ‘diskoseismic’ models in which the 300 Hz QPO is attributed to g-mode or c-mode oscillations trapped in the inner accretion disk (Nowak & Wagoner 1992,1993; Perez et al. 1997), because these models also require a rapidly rotating black hole with $a_* \sim 0.95$ and $a_* \sim 0.85$, respectively (Wagoner 1998).

Finally, we investigate the relationship between the derived spectral parameters and the intermediate, variable frequency QPOs (14–28 Hz) in GRO J1655–40. Figures 9a & b illustrate a surprising correlation between QPO frequency, r_{eff} , and the 2–100 keV power-law flux for the variable frequency (14–28 Hz) QPOs. Figure 9a shows that the QPO frequency decreases as r_{eff} decreases, which is contrary to the behavior expected if the QPO were tied to the Keplerian frequency at the shrinking inner edge of the disk.

7. Summary & Conclusion

We have analyzed RXTE data obtained for GRO J1655–40 covering a complete, 16-month outburst cycle of the source. These data comprise a nearly continuous observation

of the source with the ASM, and 52 pointed observations with the PCA and HEXTE instruments. Satisfactory fits to nearly all the PCA/HEXTE data were obtained with a multicolor blackbody disk plus power-law model (with allowance for some minor modifications). The source exhibits two principal outburst states which we associate with the very high and high/soft states. During the very high state, the spectrum was often dominated by a power-law component with $\Gamma = 2.3\text{--}2.7$. The source exhibited intense flares which were correlated with changes (hours to days) in both the fitted temperature and radius of the inner accretion disk. During the high/soft state, the spectrum was dominated by the soft thermal emission from the accretion disk with approximately constant inner disk radius and temperature. The power-law component was relatively weak with $\Gamma \sim 2\text{--}3$. During the last few observations, the source underwent a transition to the low/hard state.

We found that a tight relationship exists between the observed inner radius of the disk and the flux in the power-law component (Fig. 7b). During intense hard flares, the effective inner disk radius is observed to decrease by as much as a factor of three (from 5.5 to $1.6 r_g$) on a time scale of days. The apparent decrease of the inner disk radius observed in GRO J1655–40 during periods of increased power-law emission may be explained by the failure of the multicolor disk model due to steepening of the radial temperature profile of the accretion disk coupled with increased spectral hardening and not physical changes of the inner disk radius. This interpretation is consistent with the correlation between r_{eff} and the power-law flux (Fig. 7b) and implies that the physical mechanism responsible for producing the power-law emission is linked to the inner disk region. The same correlation between the inner disk radius and power-law flux is also evident in the spectral results for Nova Muscae 1991 presented by Ebisawa et al. (1994) and illustrated here (Fig. 8b).

Assuming that our spectral model is valid during periods of weak power-law emission, our most likely value for the inner disk radius implies $a_* < 0.7$. Such a low value for the black hole angular momentum in GRO J1655–40 is inconsistent with the relativistic frame dragging and the ‘diskoseismic’ models for the 300 Hz QPO, because these models require a rapidly rotating black hole with $a_* \sim 0.95$ and $a_* > 0.85$, respectively.

Partial support for J.M. and G.S. was provided by the Smithsonian Institution Scholarly Studies Program. R.R. was supported, in part, by NASA grant NAG5-3680. C.B. acknowledges support from NSF grant AST 9730774. G.S. and J.M. wish to thank D. Psaltis, A. Esin, S. Kenyon, R. Narayan, and J. Grindlay for helpful discussions, L. Titarchuk for his constructive correspondence, and an anonymous referee for constructive criticism. This research has made use of data obtained through the High Energy Astrophysics Science Archive Research Center Online Service, provided by the NASA/Goddard Space Flight Center.

As we were completing the revision of this manuscript, Shahbaz et al. (MNRAS, in press) presented additional radial velocities of GRO J1655–40 obtained during quiescence. They derive an optical mass function of $f(M) = 2.73 \pm 0.09 M_\odot$ (compared to $3.24 \pm 0.09 M_\odot$ reported by Orosz & Bailyn (1997)). The implied black hole mass would then be $6.0 \pm 0.2 M_\odot$ (using the mass ratio and inclination given by Orosz & Bailyn (1997)), rather than $7.0 \pm 0.2 M_\odot$. The main conclusions of this work (the correlation between fitted inner disk radius and power-law flux, etc) are independent of the assumed black hole mass. However, since the effective radius of the inner disk scales inversely with the black hole mass, a smaller black hole mass would imply a larger inner disk radius and hence a lower angular momentum for the black hole (i.e. $a_* < 0.6$ for $M = 6 M_\odot$).

REFERENCES

- Bailyn, C. D., et al. 1995, *Nature*, 374, 701
- Bardeen, J. M., Press, W. H. & Teukolsky, S. A. 1972, *ApJ*, 178, 347
- Belloni, T., Mendez, M., van der Klis, M., Hasinger, G., Lewin, W. H. G., & van Paradijs, J. 1996, *ApJ*, 472, L107
- Belloni, T., Mendez, M., King, A. R., van der Klis, M., & van Paradijs, J. 1997a, *ApJ*, 479, L145
- Belloni, T., Mendez, M., King, A. R., van der Klis, M., & van Paradijs, J. 1997b, *ApJ*, 488, L109
- Cui, W., Zhang, S. N. & Chen, W. 1998, *ApJ*, 492, 53.
- Done, C., Mulchaey, J. S., Mushotzky, R. F., & Arnaud, K. A. 1992, *ApJ*, 395, 275
- Ebisawa, K., Ogawa, M., Aoki, T., Dotani, T., Takizawa, M., Tanaka, Y., Yoshida, K., Miyamoto, S., Iga, S., Hayashida, K., Kitamoto, S., & Terada, K. 1994, *PASJ*, 46, 375
- Esin, A. A., McClintock, J. E., & Narayan, R. 1997a, *ApJ*, 489, 865
- Esin, A. A., Narayan, R., Cui, W., Grove, J. E., & Zhang, S. N. 1997b, *ApJ*, submitted, astro-ph/9711167
- Frank, J., King, A. & Raine, D. 1992, *Accretion Power in Astrophysics*, Cambridge University Press, Cambridge, p. 78
- Hameury, J.-M., Lasota, J.-P., McClintock, J. E. & Narayan, R. 1997, 489, 234
- Hjellming, R. M. & Rupen, M. P. 1995, *Nature*, 375, 464
- Inoue, H. 1991, in *Frontiers of X-ray Astronomy*, ed. Y. Tanaka & K. Koyama (Tokyo: Universal Academy Press), 291
- Kalogera, V. & Baym, G. 1996, *ApJ*, 470, L61
- Levine, A. M., Bradt, H., Cui, W., Jernigan, J. G., Morgan, E. H., Remillard, R., Shirey, R. E., & Smith, D. A. 1996, *ApJ*, 469, 33
- Lightman, A. P. & Eardley, D. M. 1974, *ApJ*, 187, L1
- Magdziarz, P. & Zdziarski, A. A. 1995, *MNRAS*, 273, 837
- Makishima, K., Maejima, Y., Mitsuda, K., Bradt, H. V., Remillard, R. A., Tuohy, I. R., Hoshi, R., & Nakagawa, M. 1986, *ApJ*, 308, 635
- McClintock, J. E. 1998, in *Accretion Processes in Astrophysical Systems*, ed. S. S. Holt & T. Kallman (Woodbury, NY: AIP), 290

- Mendez, M. & van der Klis, M. 1997, *ApJ*, 479, 926
- Mioduszewski, A. J., Hjellming, R. M., Rupen, M. P., McCollough, M., Waltman, E. B., & Poollet, G. G. 1997, *BAAS*, 29, 1387
- Mirabel, I. F. & Rodriguez, L. F. 1994, *Nature*, 371, 46
- Mirabel, I. F. & Rodriguez, L. F. 1998, *Nature*, 392, 673
- Mitsuda, K., Inoue, H., Koyama, K., Makishima, K., Matsuoka, M., Ogawara, Y., Shibasaki, N., Suzuki, K., Tanaka, Y., & Hirano, T. 1984, *PASJ*, 36, 741
- Morgan, E. H., Remillard, R. A., & Greiner, J. 1997, *ApJ*, 482, 993
- Morrison, R. & McCammon, D. 1983, *ApJ*, 270, 119
- Narayan, R. & Yi, I. 1994, *ApJ*, 428, 13
- Narayan, R., Barret, D., & McClintock, J. E. 1997, *ApJ*, 482, 448
- Newell, S. J., Garrett, M. A., & Spencer, R. E. 1998, *MNRAS*, 293, L17
- Nowak, M. A. 1995, *PASP*, 107, 1207
- Nowak, M. A. & Wagoner, R. V. 1992, *ApJ*, 393, 697
- Nowak, M. A. & Wagoner, R. V. 1993, *ApJ*, 418, 187
- Orosz, J. A., Remillard, R. A., Bailyn, C. D., & McClintock, J. E. 1997, *ApJ*, 478, L83
- Orosz, J. A. & Bailyn, C. D. 1997, *ApJ*, 477, 876
- Page, D. N. & Thorne, K. S. 1974, *ApJ*, 191, 499
- Perez, C. A., Silbergleit, A. S., Wagoner, R. V., & Lehr, D. E. 1997, *ApJ*, 476, 589
- Remillard, R. A., Morgan, E. H., McClintock, J. E., Bailyn, C. D., Orosz, J. A., & Greiner, J., 1997, to appear in *Annals of the N. Y. Academy of Sciences*, presented at the 18th Texas Symposium
- Remillard, R. A., Morgan, E. H., McClintock, J. E., Bailyn, C. D., & Orosz, J. A. 1998, *ApJ*, in press
- Shakura, N. I. & Sunyaev, R. A. 1973, *A&A*, 24, 337
- Shimura, T. & Takahara, F. 1995, *ApJ*, 445, 780
- Shrader, C. & Titarchuk, L. 1998, *ApJ*, 499, L31
- Smith, D. M., Heindl, W. A., Swank, J., Leventhal, M., Mirabel, I. F. & Rodriguez, L. F. 1997, *ApJ*, 489, L51
- Tanaka, Y. & Lewin, W. H. G. 1995, in *X-ray Binaries*, ed. W. H. G. Lewin, J. van Paradijs, & E. P. J. van den Heuvel (Cambridge: Cambridge Univ. Press)

- Tanaka, Y. & Shibazaki, N. 1996, *ARA&A*, 34, 607
- Tingay, S. J. et al. 1995, *Nature*, 374, 141
- van der Hooft, F., Heemskerk, M. H. M., Alberts, F., & van Paradijs, J. 1998, *A&A*, 329, 538
- van der Klis, M. 1995, in *X-ray Binaries*, ed. W. H. G. Lewin, J. van Paradijs, & E. P. J. van den Heuvel (Cambridge: Cambridge Univ. Press)
- Wagoner, R. V. 1998, astro-ph/9805028, To be published in *Physics Reports*, proceedings of the conference *Astrophysical Fluids: From Atomic Nuclei to Stars and Galaxies*
- Zhang, S. N., et al. 1994, *IAU Circ.* 6046
- Zhang, S. N. et al. 1996, *IAU Circ.* 6462
- Zhang, S. N., Cui, W., & Chen, W. 1997a, *ApJ*, 482, L155
- Zhang, S. N., Ebisawa, K., Sunyaev, R., Ueda, Y., Harmon, B. A., Sazonov, S., Fishman, G. J., Inoue, H., Paciesas, W. S., & Takahashi, T. 1997b, *ApJ*, 479, 381

Fig. 1.— (a) The 2–12 keV ASM lightcurve (counts s^{-1}) and (b) the ratio of the ASM count rates (5–12 keV)/(3–5 keV) for GRO J1655–40. The labels in the top panel and the dashed vertical lines indicate different outburst states (see text). The small, solid vertical lines in the top panel indicate the times of pointed RXTE observations. The individual ASM dwells are plotted in (a) and the ratios of the one-day averages are plotted in (b).

Fig. 2.— Representative spectra from each of the observed spectral states of GRO J1655–40, along with the best fit model for (a, b) the very high state, (c, d) the high/soft state, and (e) the low/hard state. The individual components of the model are also shown. The 6-digit number in the upper left hand corner of each panel identifies the date of the observation (see Table 1). See the text for details on the spectral models and fitting. Although error bars are plotted for all the data, they are only large enough to be visible at the highest energies.

Fig. 3.— Spectral parameters for PCA/HEXTE observations of GRO J1655–40. The spectra were fit to a model of interstellar absorption plus multicolor blackbody disk plus power-law. The hydrogen column density was fixed at $0.89 \times 10^{22} \text{ cm}^{-2}$ (Zhang et al. 1997b). The quantities plotted here are (a) the effective temperature of the accretion disk (T_{eff}) in keV, (b) the effective inner disk radius r_{eff} in units of $r_g = GM/c^2$ for $M = 7.02M_{\odot}$, $\theta = 69^{\circ}.5$ (Orosz & Bailyn 1997), and $D = 3.2 \text{ kpc}$ (Hjellming & Rupen 1995) (see Eq. (1)), (c) the power-law photon index Γ , and (d) the power-law normalization K in units of photons $s^{-1} \text{ cm}^{-2} \text{ keV}^{-1}$ at 1 keV. The presence of the 300 Hz QPO is indicated by an open triangle and the presence of the variable frequency QPOs (14–28 Hz) is indicated by an open square at the top of (b) (Remillard et al. 1998). Here and in several subsequent figures for which error bars are not visible, it is because they are comparable to or smaller than the plotting symbol.

Fig. 4.— Effect of the Fe absorption edge on the ratio data/model for a representative high/soft state spectrum (970320). Figure (a) shows the residuals for the interstellar absorption plus multicolor blackbody disk plus power-law only. Figures (b) & (c) show the effects of a smeared Fe absorption edge applied to the power-law component (Ebisawa et al. 1994) at edge energies of 7.1 and 8.0 keV, respectively. The width of the absorption feature was kept fixed at 7 keV and the Fe optical depth was allowed to float.

Fig. 5.— Plot of (a) the total unabsorbed flux of GRO J1655–40, (b) the bolometric flux from the disk blackbody calculated using the formula: $Flux = 2\sigma ((R_{col}^2/D^2) \cos \theta) T_{col}^4$, and (c) the 2–100 keV flux from the power-law component. The units are $10^{-8} \text{ ergs s}^{-1} \text{ cm}^{-2}$. The ratio of the disk blackbody to the total unabsorbed flux is shown in (d). The total and power-law fluxes for the ten poorly-fit high/soft state spectra have been omitted because of uncertainty in the nature of the quasi-power-law component. Reducing the lower energy

bound from 2 keV to 1 keV increases the power-law fluxes by $\sim 50\%$.

Fig. 6.— Plot of (a) r_{eff} vs. l and (b) Γ vs. l , where l is the bolometric disk luminosity plus the 2–100 keV power-law luminosity in Eddington units ($L_{Edd} = 8.8 \times 10^{38}$ erg s $^{-1}$ for $M = 7.02M_{\odot}$). Data during the very high state are plotted as filled circles and data during the high/soft state are plotted as open squares. The last three data points on days 476, 480, and 487 have been omitted from (a) because the multicolor disk model no longer yields reasonable physical values for the inner disk radius. These three data points are plotted as open triangles in (b). The data points for the ten poorly-fit high/soft state spectra have been omitted from both (a) & (b) because of uncertainty in the nature of the quasi-power-law component.

Fig. 7.— Plot of (a) T_{eff} vs. r_{eff} and (b) 2–100 keV power-law flux vs. r_{eff} . Observations during the very high state are plotted as filled circles and observations during the high/soft state are plotted as open squares. The last three observations on days 476, 480, and 487 have been omitted because the multicolor disk model no longer yields reasonable physical values for the inner disk radius. The data points for the ten poorly-fit high/soft state spectra have been omitted because of uncertainty in the nature of the quasi-power-law component.

Fig. 8.— Plot of (a) T_{eff} vs. r_{eff} and (b) 2–100 keV power-law flux vs. r_{eff} for Nova Muscae 1991. This figure should be compared to Figure 7 for GRO J1655–40. r_{eff} is in units of $r_g = GM/c^2$ where $M = 6M_{\odot}$, $\theta = 60^{\circ}$ (Orosz et al. 1996), and $D = 2.5$ kpc (Ebisawa et al. 1994). Following Ebisawa et al. (1994) and for the purposes of this illustration we adopt $D = 2.5$ kpc. However, the actual distance is probably closer to twice this value (see § 4.1 in Esin et al. 1997), which would double the value of r_{eff} .

Fig. 9.— Correlation between (a) QPO frequency and r_{eff} and (b) QPO frequency and the 2–100 keV power-law flux for 14–28 Hz QPOs. The 28.3 Hz QPO plotted with a triangle appears only in the sum of the high/soft state observations (days 255–465) (Remillard et al. 1998), and is plotted here at the average r_{eff} and power-law flux for the high/soft state.

Table 1. Spectral Parameters for GRO J1655–40^a

Date (yyymmdd UT)	Day ^b (MJD 50198+)	T_{eff} (keV)	r_{eff} (r_g) ^c	Photon Index	Power-law Norm. (phot s ⁻¹ cm ⁻² keV ⁻¹ at 1 keV)	τ_{Fe} ^d	χ^2_ν (dof)	Energy Range ^e (keV)
960509	14.8	0.73 ± 0.01^f	6.42 ± 0.04^f	$5.77^{+0.21}_{-0.19}g$	$4620^{+3640}_{-1900}g$	–	1.65(39) ^f	–
960510	15.5	0.72 ± 0.01^f	6.57 ± 0.04^f	$6.47^{+0.33}_{-0.20}g$	$31400^{+47100}_{-13100}g$	–	1.13(39) ^f	–
960511	16.5	0.73 ± 0.01^f	6.48 ± 0.04^f	$5.69^{+0.30}_{-0.26}g$	$3930^{+5210}_{-2030}g$	–	1.45(39) ^f	–
960512	17.4	0.73 ± 0.01^f	6.36 ± 0.05^f	$5.75^{+0.32}_{-0.26}g$	$4900^{+7140}_{-2530}g$	–	1.13(39) ^f	–
960725	91.4	0.77 ± 0.01	5.37 ± 0.04	2.28 ± 0.01	5.90 ± 0.18	–	1.57(248)	2.5-100
960801 ^h	98.4	1.13 ± 0.01	1.64 ± 0.06	2.68 ± 0.01	62.7 ± 1.3	–	1.35(246)	2.5-100
960806	103.7	0.93 ± 0.01	2.70 ± 0.05	2.67 ± 0.01	44.1 ± 0.9	–	0.84(248)	2.5-100
960815	112.6	0.76 ± 0.01	5.35 ± 0.04	2.30 ± 0.02	$5.90^{+0.37}_{-0.35}$	–	2.11(150)	2.5-50
960816	113.4	0.78 ± 0.01	4.49 ± 0.07	2.42 ± 0.01	18.9 ± 0.6	–	1.23(248)	2.5-100
960822	119.5	0.76 ± 0.01	4.96 ± 0.05	2.46 ± 0.01	16.4 ± 0.5	–	0.88(248)	2.5-100
960829 ^h	126.4	1.09 ± 0.01	$1.98^{+0.07}_{-0.09}$	2.78 ± 0.03	$65.5^{+2.4}_{-2.2}$	–	0.73(246)	2.5-50
960904	132.3	0.76 ± 0.01	5.34 ± 0.05	2.40 ± 0.02	$9.59^{+0.43}_{-0.41}$	–	1.89(150)	2.5-50
960909	138.0	0.78 ± 0.01	5.07 ± 0.05	2.37 ± 0.01	9.49 ± 0.22	–	1.50(248)	2.5-100
960920	148.2	0.75 ± 0.01	5.44 ± 0.04	2.23 ± 0.02	$4.31^{+0.23}_{-0.22}$	–	1.60(150)	2.5-50
960926	154.3	0.75 ± 0.01	5.72 ± 0.04	1.97 ± 0.03	$0.93^{+0.07}_{-0.06}$	–	1.32(150)	2.5-50
961003	161.6	0.75 ± 0.01	5.65 ± 0.04	2.14 ± 0.02	$2.16^{+0.13}_{-0.12}$	–	0.82(150)	2.5-50
961015	173.5	0.78 ± 0.01	5.39 ± 0.04	2.18 ± 0.01	3.83 ± 0.13	–	1.09(248)	2.5-100
961022	180.1	0.77 ± 0.01	5.55 ± 0.05	2.23 ± 0.01	4.86 ± 0.15	–	0.92(248)	2.5-100
961027	185.6	0.80 ± 0.01	4.56 ± 0.06	2.59 ± 0.02	26.0 ± 1.5	–	0.60(91)	2.5-20
961102A ^h	191.2	$0.84^{+0.01}_{-0.02}$	$2.15^{+0.10}_{-0.09}$	2.57 ± 0.01	35.9 ± 0.8	–	1.26(246)	2.5-100
961102B ^h	191.3	1.09 ± 0.01	$1.69^{+0.07}_{-0.09}$	2.64 ± 0.01	$53.4^{+1.9}_{-1.5}$	–	1.00(246)	2.5-100
970105	255.4	0.64 ± 0.01	$5.72^{+0.07}_{-0.06}$	1.94 ± 0.04	$0.92^{+0.13}_{-0.12}$	0.40 ± 0.25	1.08(149)	2.5-50
970112	262.1	0.62 ± 0.01	6.27 ± 0.07	2.00 ± 0.06	0.61 ± 0.13	0.97 ± 0.33	0.88(149)	2.5-50
970121	271.0	0.55 ± 0.01	6.50 ± 0.05	1.65 ± 0.09	0.03 ± 0.01	$0.00^{+2.97}_{-0.00}$	0.82(91)	2.5-20
970126	276.9	0.57 ± 0.01	6.65 ± 0.10	2.17 ± 0.10	$0.48^{+0.16}_{-0.13}$	$1.79^{+0.42}_{-0.48}$	0.56(90)	2.5-20
970226	307.9	0.65 ± 0.01	6.62 ± 0.05	3.01 ± 0.08	$4.50^{+1.06}_{-0.92}$	10.2 ± 0.4	2.53(107)	2.5-30
970305	314.8	0.66 ± 0.01	6.70 ± 0.06	2.96 ± 0.08	$4.89^{+1.15}_{-1.00}$	7.23 ± 0.32	2.20(90)	2.5-20
970310	319.7	0.66 ± 0.01	6.61 ± 0.05	2.75 ± 0.08	$3.46^{+0.89}_{-0.76}$	$5.64^{+0.29}_{-0.31}$	1.53(90)	2.5-20
970320	329.9	0.67 ± 0.01	6.63 ± 0.04	2.43 ± 0.07	$1.99^{+0.50}_{-0.42}$	$3.62^{+0.30}_{-0.32}$	1.04(147)	2.5-49
970324	333.8	0.67 ± 0.01^f	6.61 ± 0.03^f	$2.70^{+0.40}_{-0.35}g$	$0.61^{+1.26}_{-0.61}g$	–	2.58(39) ^f	–
970404	344.7	0.67 ± 0.01	6.64 ± 0.04	2.41 ± 0.09	$1.88^{+0.54}_{-0.45}$	$3.76^{+0.32}_{-0.35}$	1.17(149)	2.5-50
970410	350.5	0.67 ± 0.01	6.58 ± 0.04	2.44 ± 0.09	$2.38^{+0.71}_{-0.60}$	$3.53^{+0.30}_{-0.33}$	0.86(90)	2.5-20
970416	356.8	0.66 ± 0.01	6.65 ± 0.05	2.96 ± 0.08	$4.19^{+1.10}_{-0.91}$	$9.03^{+0.38}_{-0.39}$	2.29(89)	2.5-20
970424	364.8	0.67 ± 0.01^f	6.58 ± 0.03^f	2.96 ± 0.65^g	$1.14^{+6.05}_{-1.14}g$	–	1.92(39) ^f	–
970430	370.6	0.68 ± 0.01^f	6.50 ± 0.03^f	3.50 ± 0.56^g	$4.76^{+18.5}_{-4.76}g$	–	2.33(39) ^f	–
970508	378.5	0.70 ± 0.01^f	6.40 ± 0.03^f	$2.87^{+0.42}_{-0.38}g$	$1.07^{+2.47}_{-1.07}g$	–	2.04(39) ^f	–
970512	382.7	0.70 ± 0.01^f	6.40 ± 0.03^f	$5.10^{+0.55}_{-0.62}g$	$387^{+1400}_{-318}g$	–	1.90(39) ^f	–
970520	390.4	0.71 ± 0.01	6.31 ± 0.06	$2.89^{+0.10}_{-0.12}$	$3.86^{+1.37}_{-1.15}$	$4.82^{+0.51}_{-0.57}$	1.43(90)	2.5-20
970528	398.4	0.71 ± 0.01	6.30 ± 0.05	2.52 ± 0.08	$3.08^{+0.80}_{-0.68}$	$2.92^{+0.33}_{-0.35}$	0.91(147)	2.5-49
970605	406.3	0.69 ± 0.01	6.38 ± 0.06	2.86 ± 0.09	$4.71^{+1.30}_{-1.16}$	$4.73^{+0.36}_{-0.20}$	1.10(108)	2.5-30
970609	410.5	0.68 ± 0.01	6.49 ± 0.07	2.89 ± 0.11	$4.24^{+1.47}_{-1.24}$	$6.59^{+0.47}_{-0.51}$	1.10(90)	2.5-20
970619	420.3	0.67 ± 0.01	6.56 ± 0.04	2.24 ± 0.11	$1.38^{+0.47}_{-0.40}$	$3.39^{+0.33}_{-0.40}$	0.80(90)	2.5-20
970626	427.8	0.65 ± 0.01^f	6.71 ± 0.03^f	$3.35^{+0.76}_{-0.73}g$	$3.13^{+23.3}_{-3.13}g$	–	0.95(39) ^f	–
970704	435.5	0.61 ± 0.01	6.95 ± 0.04	2.64 ± 0.09	$1.82^{+0.52}_{-0.44}$	$6.10^{+0.27}_{-0.30}$	1.51(90)	2.5-20
970708	439.6	0.62 ± 0.01	6.59 ± 0.06	2.10 ± 0.10	$0.71^{+0.23}_{-0.20}$	$2.10^{+0.38}_{-0.45}$	0.79(90)	2.5-20
970714	445.3	0.60 ± 0.01	7.11 ± 0.05	2.53 ± 0.11	$1.31^{+0.47}_{-0.38}$	$5.13^{+0.35}_{-0.39}$	0.87(90)	2.5-20
970724	455.6	0.57 ± 0.01	6.60 ± 0.08	2.16 ± 0.05	$0.67^{+0.12}_{-0.10}$	$1.94^{+0.23}_{-0.24}$	1.09(149)	2.5-50
970729	460.4	0.51 ± 0.01	6.89 ± 0.12	2.22 ± 0.05	$0.94^{+0.13}_{-0.12}$	2.32 ± 0.25	0.88(90)	2.5-20
970803	465.7	0.46 ± 0.01	7.31 ± 0.12	2.52 ± 0.06	$0.87^{+0.13}_{-0.12}$	2.19 ± 0.26	1.01(90)	2.5-20
970814	476.5	0.31 ± 0.02	$5.57^{+0.94}_{-0.77}$	2.00 ± 0.01	0.76 ± 0.02	0.85 ± 0.07	0.87(149)	2.5-50
970818	480.6	0.33 ± 0.04	$1.82^{+0.94}_{-0.54}$	1.71 ± 0.02	0.14 ± 0.01	0.34 ± 0.10	0.78(119)	2.5-50
970825	487.5	0.26 ± 0.03	$3.12^{+1.45}_{-0.87}$	1.89 ± 0.11	0.02 ± 0.01	$1.20^{+0.53}_{-0.52}$	0.51(74)	2.5-17

Table 1—Continued

Date (yyymmdd UT)	Day ^b (MJD 50198+)	T_{eff} (keV)	r_{eff} (r_g) ^c	Photon Index	Power-law Norm. (phot s ⁻¹ cm ⁻² keV ⁻¹ at 1 keV)	τ_{Fe} ^d	χ^2_ν (dof)	Energy Range ^e (keV)
-------------------------	-------------------------------------	-----------------	----------------------------------	-----------------	--	--------------------------	-----------------------	---------------------------------------

^aUsed fixed $N_H = 0.89 \times 10^{22}$ cm⁻² (Zhang et al. 1997).

^bMidpoint of observation.

^c $r_g = GM/c^2$ for $M = 7.02M_\odot$ and Eq. (1) with $\theta = 69^\circ 5$ (Orosz & Bailyn 1997) and $D = 3.2$ kpc (Hjellming & Rupen 1995).

^dFixed edge at 8.0 keV and width of 7 keV using ‘smedge’ model in XSPEC.

^ePCA = 2.5 – 20 keV & HEXTE > 20 keV.

^fDetermined from 2.5-10 keV using only interstellar absorption and multicolor disk blackbody models.

^gDetermined from 15-20 keV with fixed multicolor disk parameters determined from 2.5-10 keV.

^hFitted including a Compton reflection component model (see §3.1 and Table 2).

Table 2. Fit Parameters for Compton Reflection^a

Date (yymmdd UT)	Day ^b (MJD 50198+)	$\Omega/2\pi^c$	ξ^d
960801	98.4	$0.88^{+0.09}_{-0.08}$	442^{+499}_{-272}
960829	126.4	$1.30^{+0.27}_{-0.35}$	$84.5^{+642}_{-79.2}$
961102A	191.2	0.58 ± 0.07	$1.01^{+12.0}_{-0.97}$
961102B	191.3	$1.15^{+0.11}_{-0.10}$	$0.013^{+41.4}_{-0.013}$

^aThe Compton reflection component was calculated using the ‘pexriv’ model in XSPEC version 10. The Fe and elemental abundances were fixed at the solar value. The disk temperature was fixed at 10^5 K (Done et al. 1992), the inclination angle was fixed at $69^\circ.5$ (Orosz & Bailyn 1997). No exponential cutoff of the power-law was applied.

^bMidpoint of observation.

^cNormalization of reflection.

^dThe ionization parameter $\xi = L/nR^2$, where L is the integrated incident luminosity between 5 eV and 300 keV, n is the density of the material, and R is the distance of the material from the illuminating source (Done et al. 1992).

Table 3. Determining r_{last} & a_* from r_{eff}

$r_{eff} (r_g)^\dagger$	$r_{last} (r_g)^\dagger$	η	a_*
1.58	1.24	0.782	0.998
1.66	1.28	0.771	0.997
1.75	1.33	0.760	0.996
1.98	1.45	0.736	0.99
2.80	1.94	0.692	0.95
3.08	2.10	0.683	0.93
3.44	2.32	0.675	0.90
4.42	2.91	0.658	0.80
5.22	3.39	0.650	0.70
5.94	3.83	0.645	0.60
6.61	4.23	0.640	0.50
7.24	4.61	0.637	0.40
7.85	4.98	0.634	0.30
8.43	5.33	0.632	0.20
9.00	5.67	0.630	0.10
9.55	6.00	0.628	0.00

$^\dagger r_g = GM/c^2$

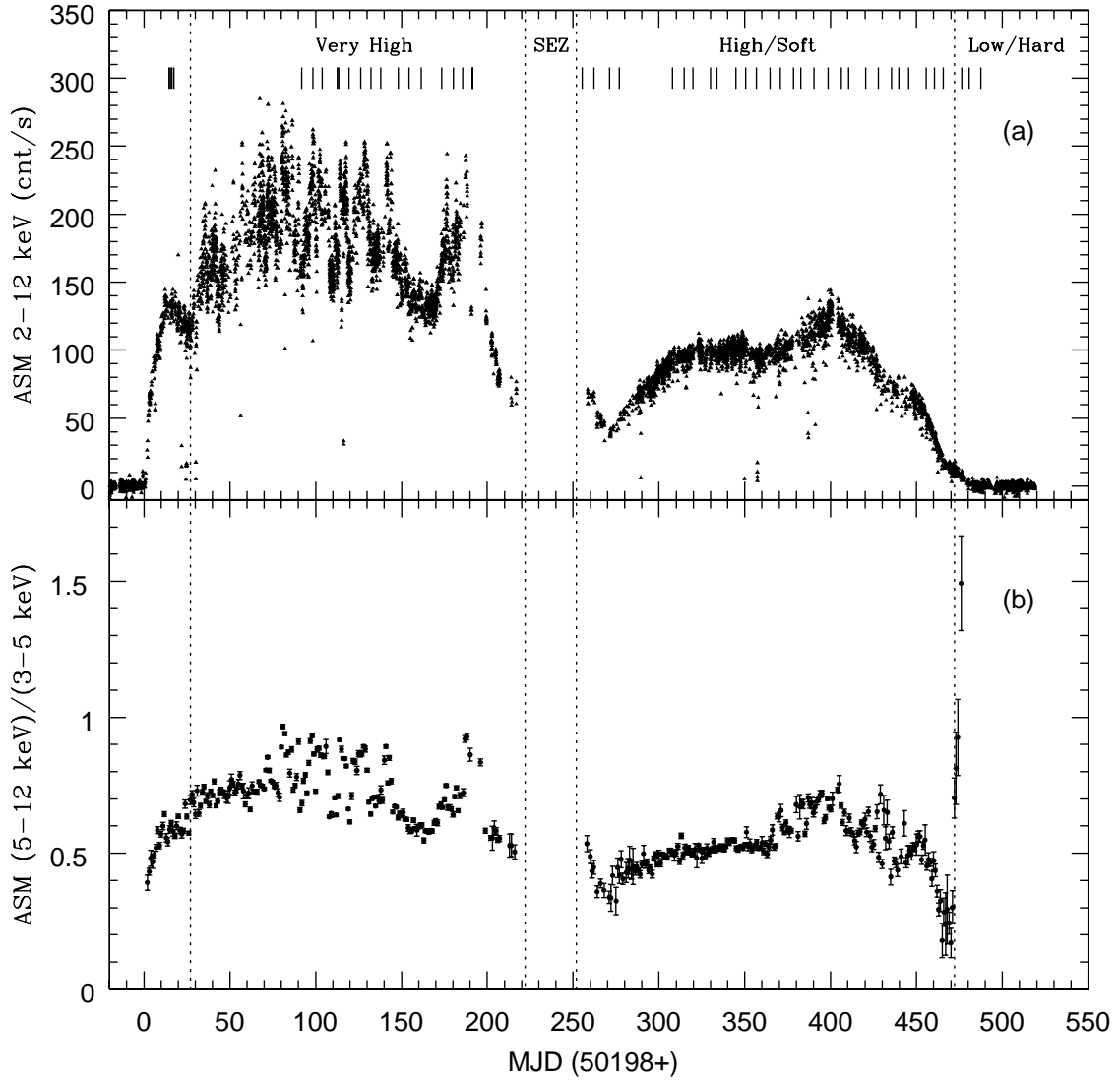


Fig. 1.—

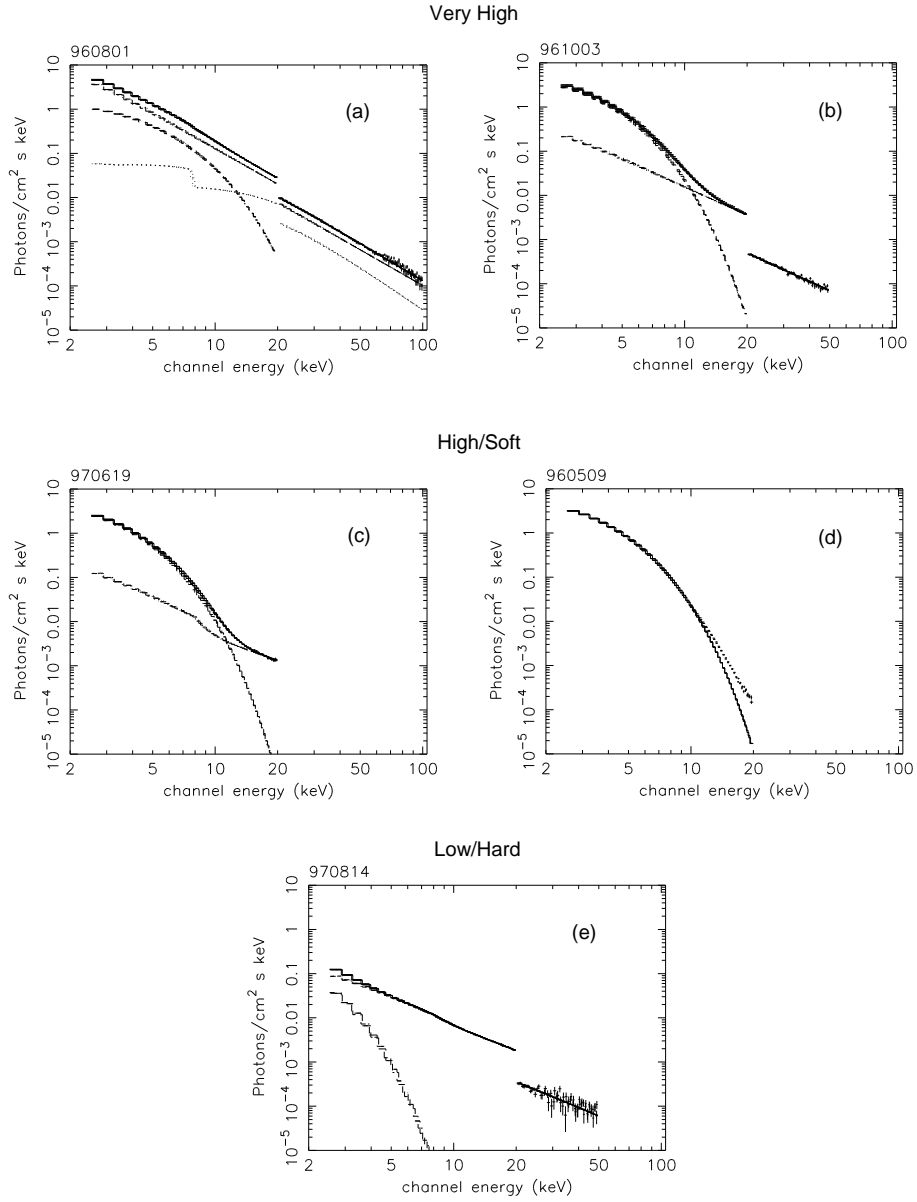


Fig. 2.—

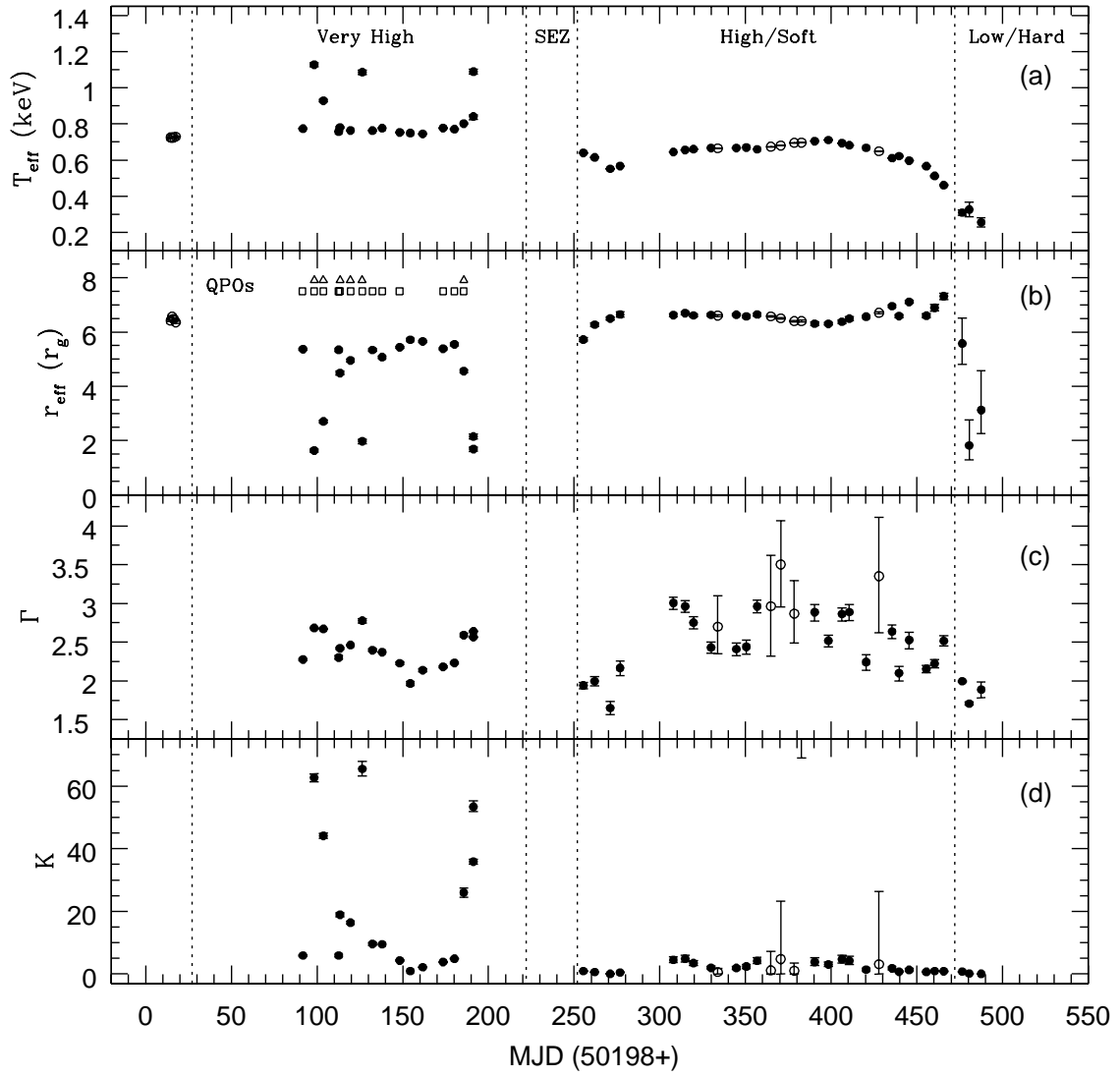


Fig. 3.—

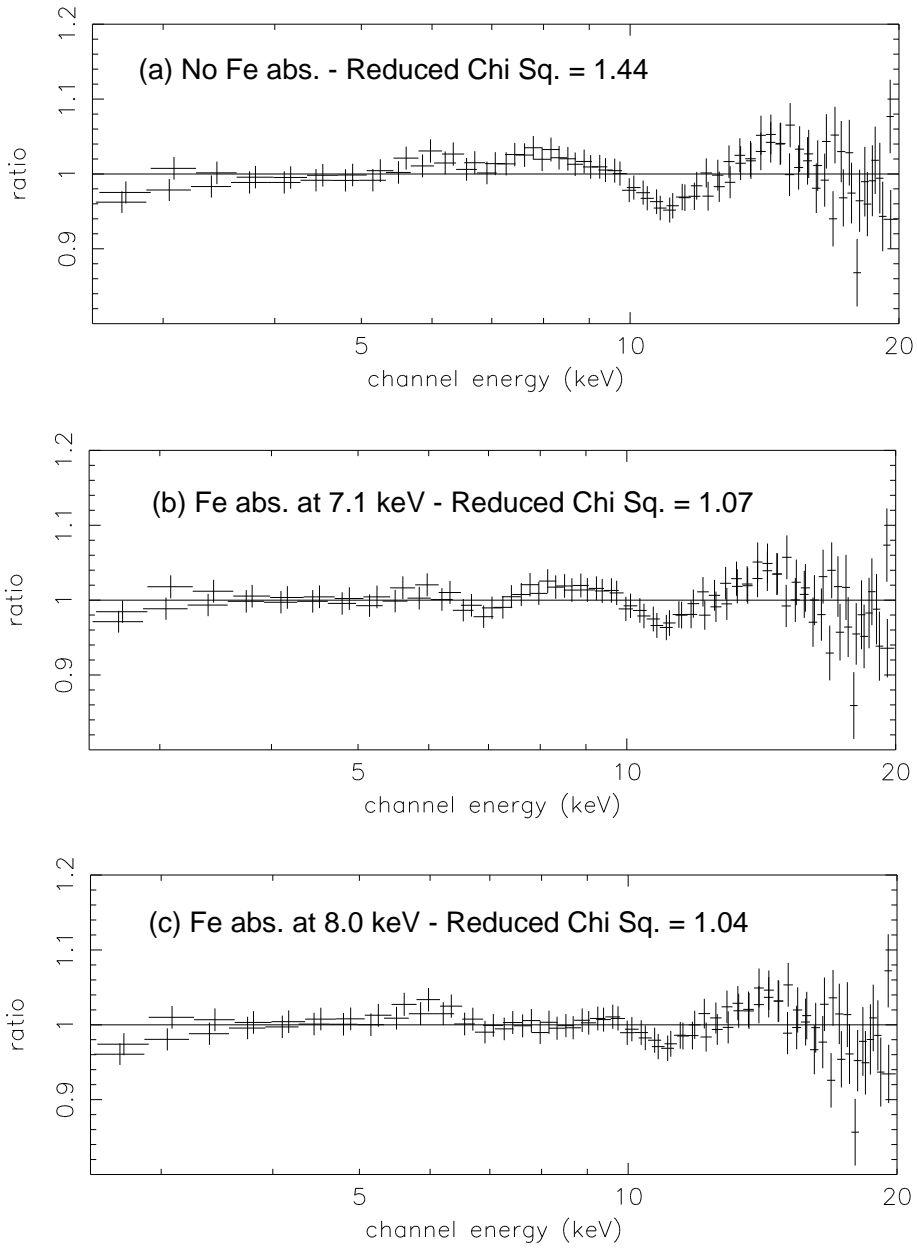


Fig. 4.—

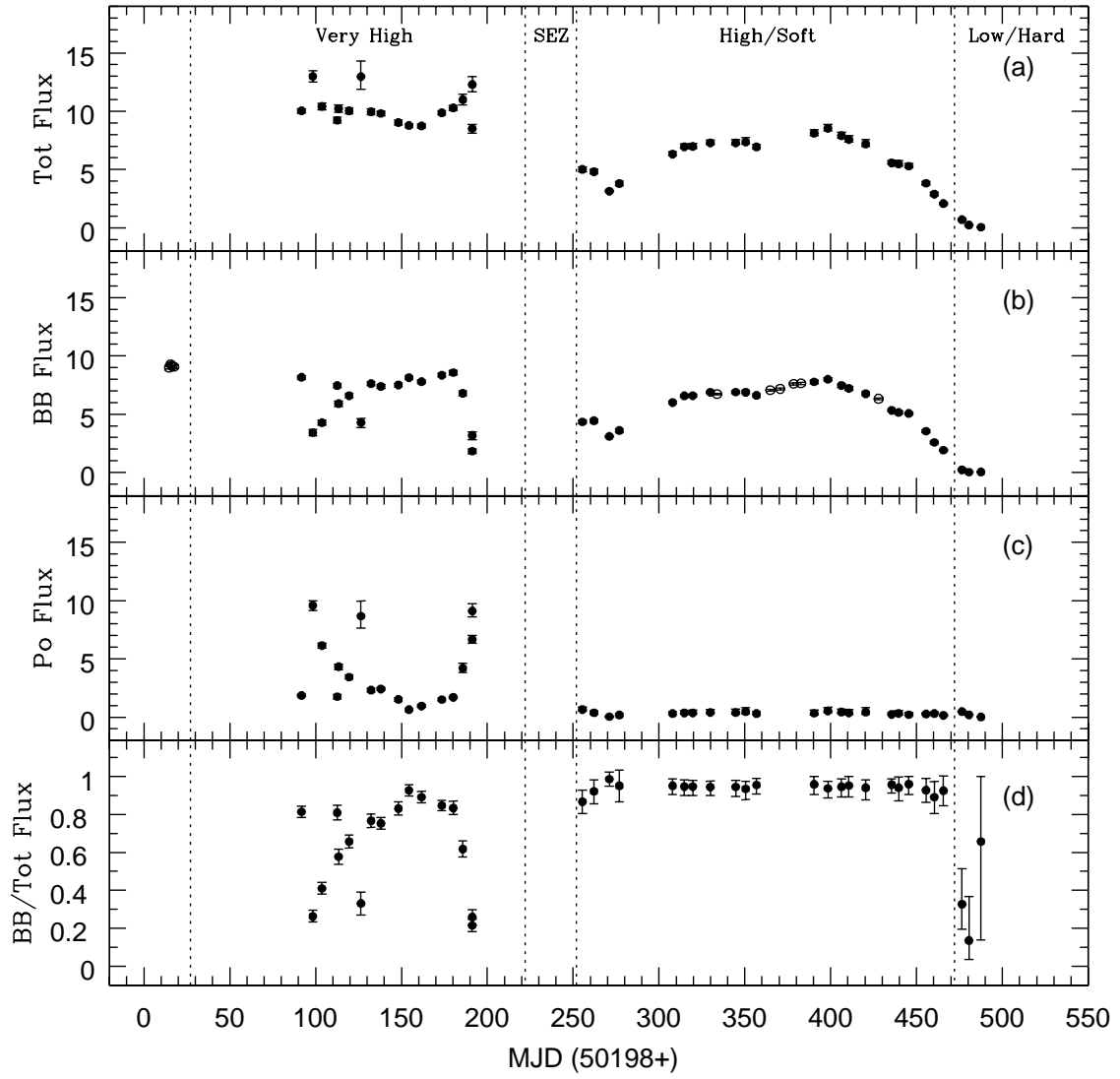


Fig. 5.—

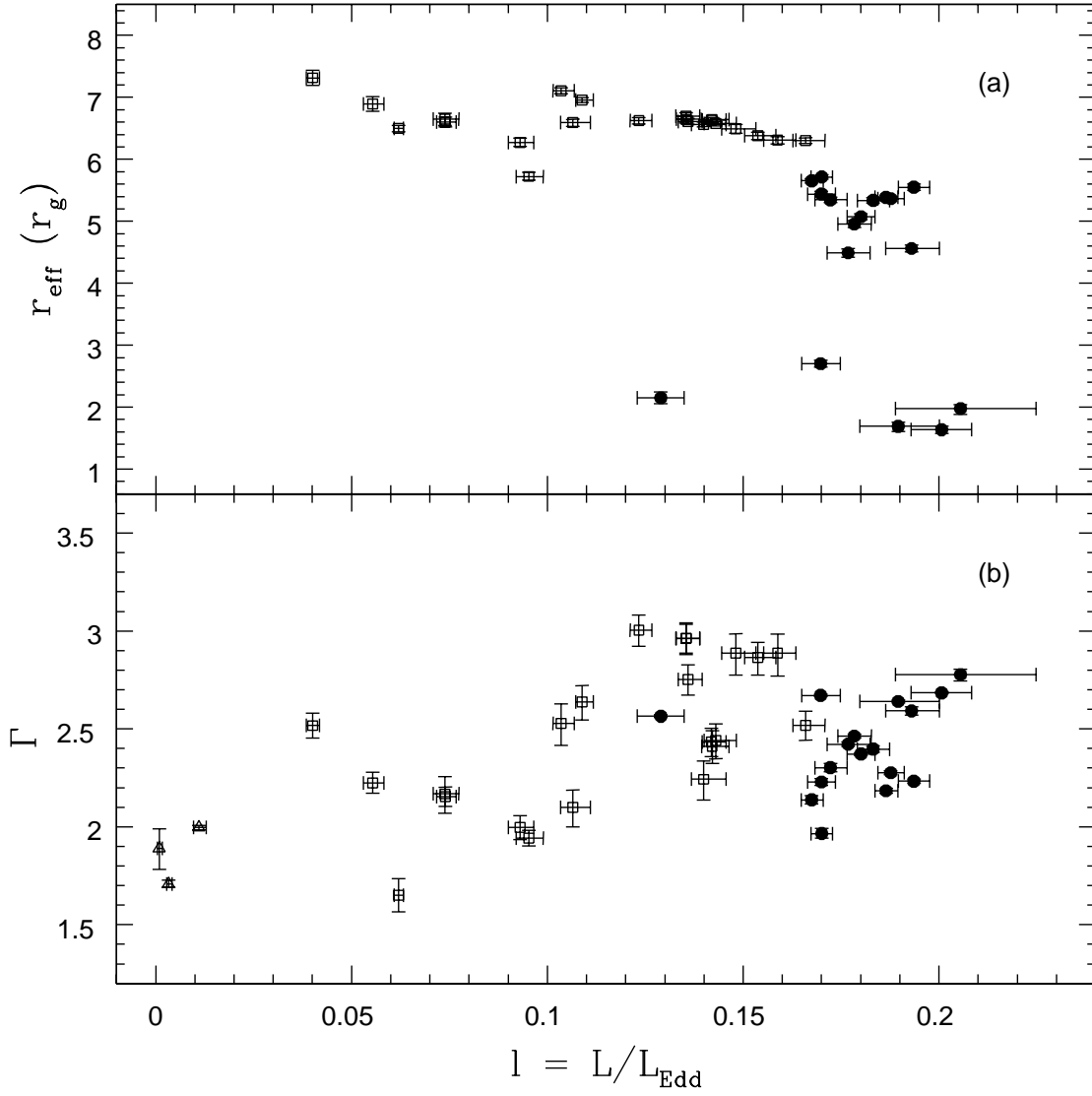


Fig. 6.—

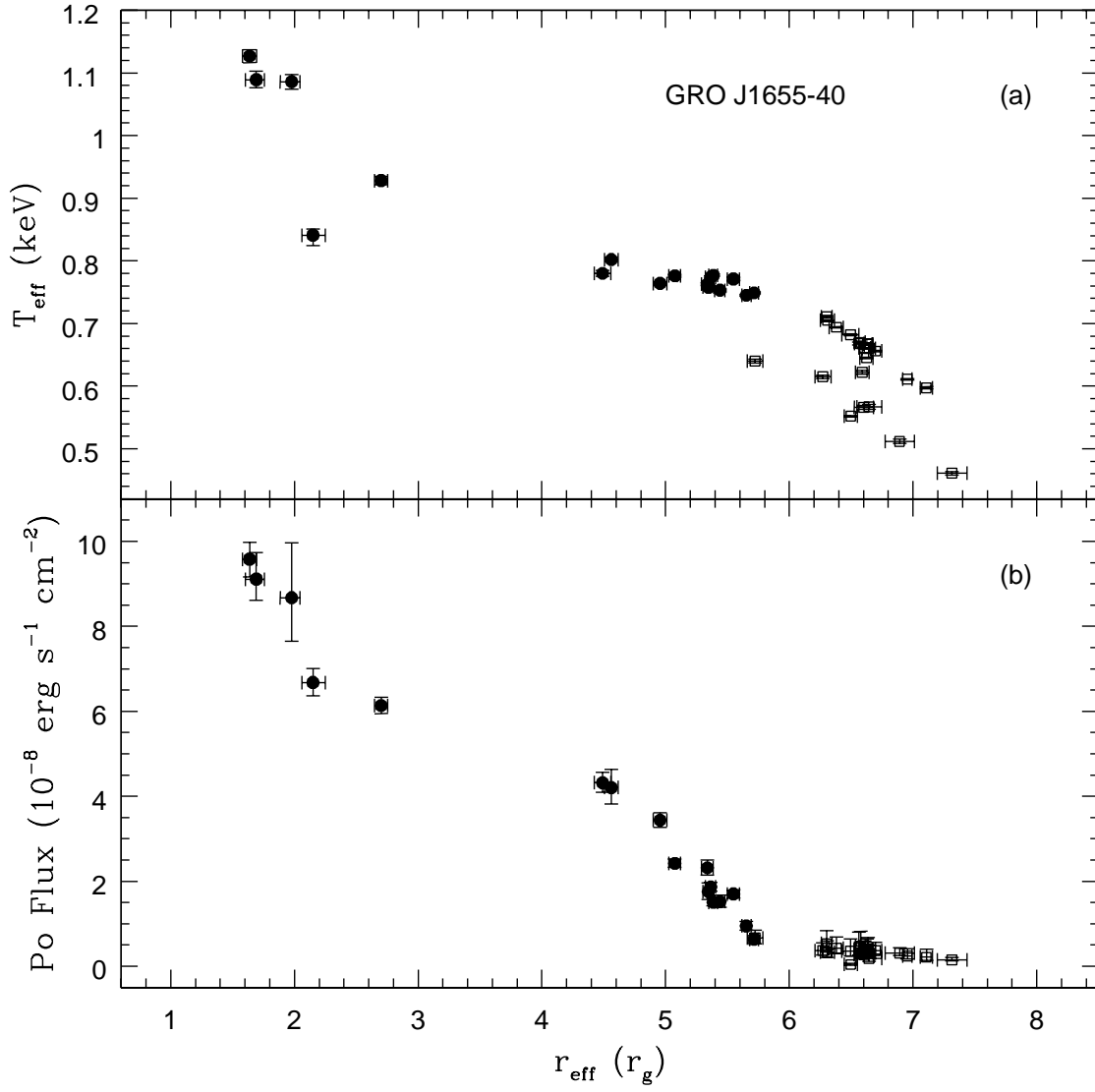


Fig. 7.—

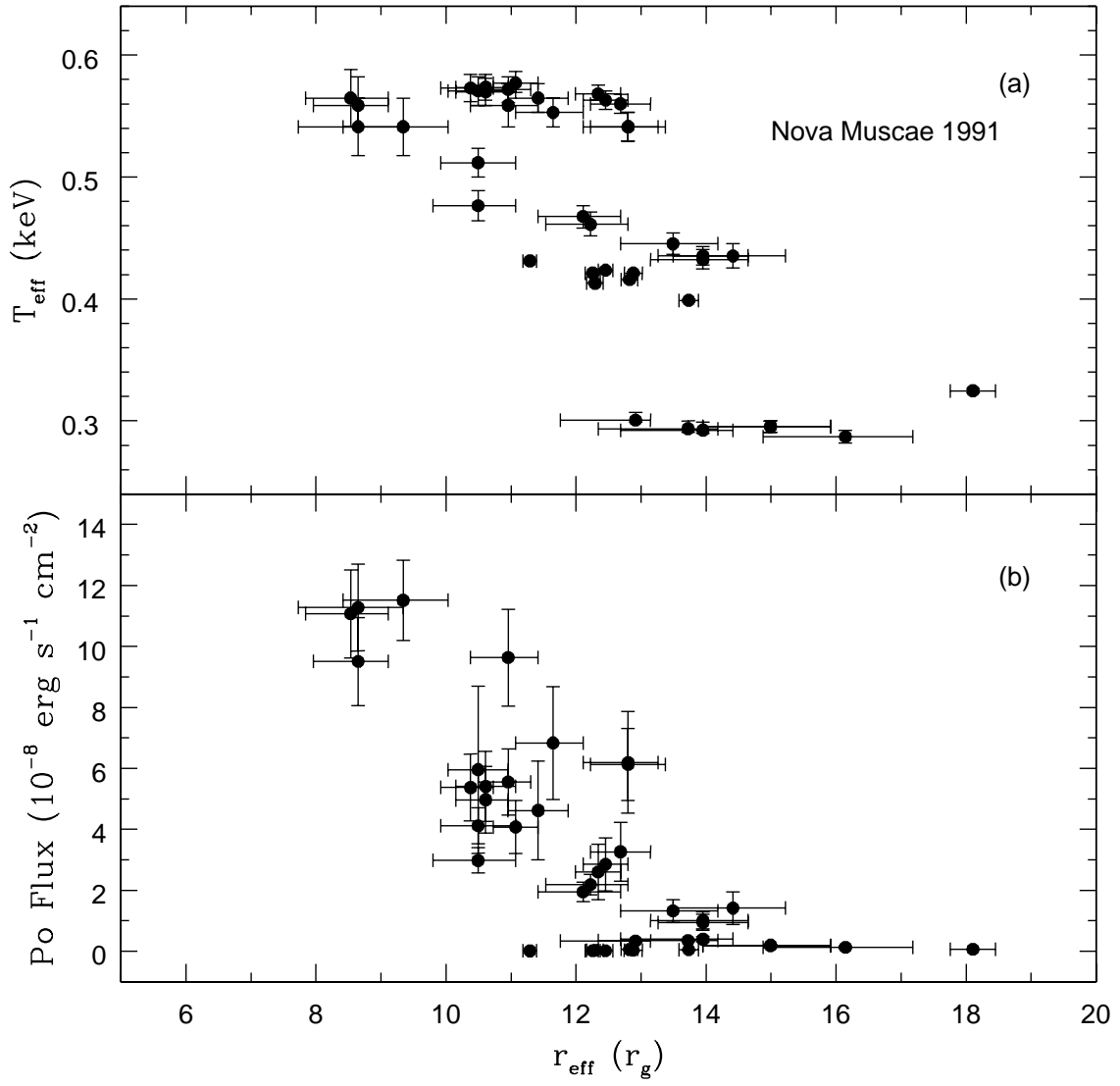


Fig. 8.—

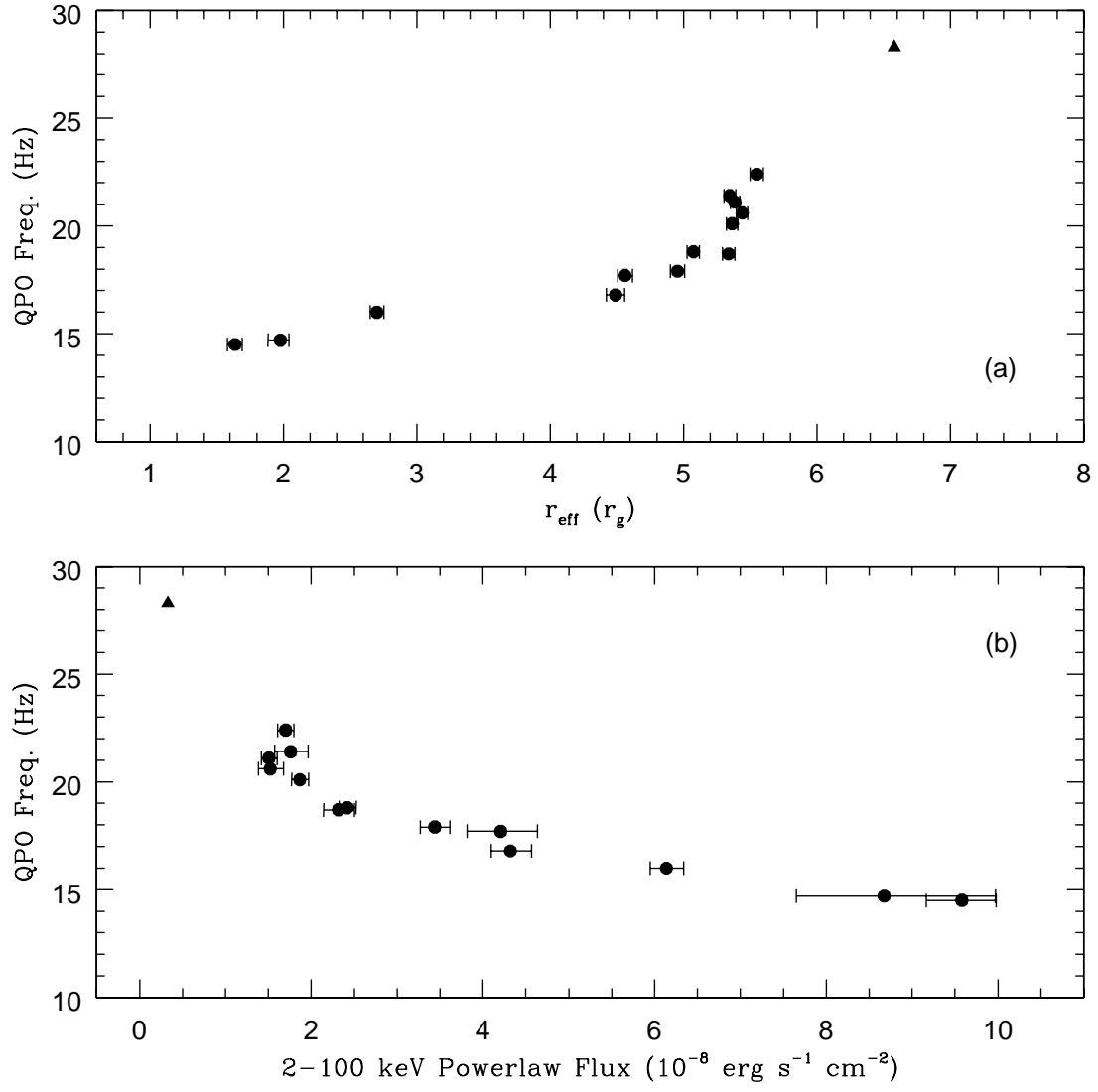


Fig. 9.—